ADVANCED OPTICAL MATERIALS
www.advopticalmat.de

Single-Threshold Amplified Spontaneous Emission in the Absence of Photon Gain in $MAPbBr_3$ Planar Waveguides

Angelica Simbula, Federico Pitzalis, Riccardo Pau, Emanuele D. Cadeddu, Luyan Wu, Stefano Lai, Fang Liu, Selene Matta, Valeria Demontis, Daniela Marongiu, Paolo Pintus, Francesco Quochi, Michele Saba, Andrea Mura, and Giovanni Bongiovanni**

Metal halide perovskites have emerged as promising materials for low-threshold lasers, ideally suited for integrated optical circuits due to their easy fabrication, tunable wavelength, and seamless on-chip integration. Exciton lasing, electron-hole population inversion, polariton condensation and superfluorescence have been proposed to explain the low threshold. Fundamental to discriminate lasing mechanisms is the knowledge of the material's absorption/gain spectrum in the stimulated emission regime, a difficult experimental task in microcavities and metasurfaces. In this study, femtosecond tandem spectroscopy applied to $MAPbBr_3$ planar waveguides enables the measurement of material absorption and gain spectra at any carrier density, as well as directly monitoring the matter component of hybrid excitations. Results demonstrate that stimulated emission always involves hybrid electron-hole-photon excitations in the absence of photon gain, even at the highest excitations when the exciton resonance is completely bleached, a characteristic almost unique in the landscape of photonic materials. Parameter-free numerical simulations show that $MAPbBr_3$ waveguides support electromagnetic modes with an exciton-polariton-like dispersion below the bandgap at all investigated carrier densities. These excitations combine the advantages of hybrid light-matter states- namely, lower stimulated emission thresholds and higher nonlinearities- with the robustness of photon amplification, seamlessly extending potential applications from low to high carrier densities.

1. Introduction

Metal halide perovskites (MHPs) are solution-processable semiconductors with tunable bandgap and high emission quantum yields that make them promising for cost-effective lasers and light amplifiers in integrated optical circuits.[1–3] Thanks to nanopatterning-based fabrication technologies, MHPs can be used to realize photonic crystals and metasurfaces, with novel topological emission properties and easy integration into optical circuit.[4–10] When optical microcavity modes are strongly coupled to excitons, they form hybrid light-matter quasiparticles known as exciton-polaritons, which profoundly modify the microscopic lasing mechanisms.[11–20] Exciton-polariton lasing occurs when polaritons accumulate in a low-energy state due to stimulated scattering from a thermal excitation reservoir, forming a non-equilibrium Bose-Einstein condensate. However, polaritons can also form without the need for optical cavity feedback, such as in bulk materials or planar waveguides (PW), the latter being the

A. Simbula, F. Pitzalis, R. Pau, E. D. Cadeddu, L. Wu, S. Lai, F. Liu, S. Matta, V. Demontis, D. Marongiu, P. Pintus, F. Quochi, M. Saba, A. Mura, G. Bongiovanni
Dipartimento di Fisica
Università degli Studi di Cagliari
Monserrato, CA 09042, Italy
E-mail: angelica.simbula@dsf.unica.it; giovanni.bongiovanni@dsf.unica.it

The ORCID identification number(s) for the author(s) of this article can be found under https://doi.org/10.1002/adom.202402798

DOI: 10.1002/adom.202402798

R. Pau
Zernike Institute for Advanced Materials
University of Groningen
Nijenborgh 4, Groningen, AG 09747, The Netherlands

F. Liu
School of Environmental Science and Engineering
Frontiers Science Center for Transformative Molecules
Shanghai Jiao Tong University
Shanghai 200240, China

simplest photonic structures that can sustain light amplification.[21–26] Exciton-polariton lasing and amplification in thin films were first observed in ZnO PWs,[27] despite the absence of an energy minimum in the polariton dispersion. Unlike conventional photon lasing, exciton-polariton lasing does not require population inversion, thus starting at lower energy input and offering more energy-efficient light sources. Additionally, the matter component enhances interactions, enabling stronger nonlinear functionalities for logic operations.[18,19] Understanding the microscopic mechanisms of stimulated emission MHP PWs is crucial for their full application potential. However, despite their fundamental differences, distinguishing between exciton-polariton and photon stimulated emission is experimentally challenging.

Exciton-polariton lasing requires that exciton oscillator strength remains unchanged up to the lasing threshold. At higher photocarrier density, Coulomb screening weakens the exciton-photon interaction, causing polariton to collapse and stopping lasing. In Mott's insulator-to-metal transition framework, above the Mott density (ρ_M), excitons disappear and only unbound electrons and holes survive.[28] Population inversion and photon gain above ρ_M can trigger photon stimulated emission, resulting in a second lasing threshold. The observation of two distinct thresholds has been used as an indirect test to demonstrate that the first threshold corresponds to exciton-polariton lasing, while the second corresponds to photon lasing.[29]

The most studied MHPs for laser and light amplification applications are $MAPbBr_3$ and $CsPbBr_3$. These compounds exhibit comparable absorption spectra, indicating similar exciton binding energies and oscillator strengths. For these MHPs, the best theoretical estimate of the Mott density is $\rho_M \approx 8{\cdot}10^{17}$ cm^{-3}.[30] Polariton or photon stimulated emission is the microscopic scattering mechanism that, through an avalanche process, generates an intense polariton or photon amplified spontaneous emission (ASE) band, or a narrow line lasing emission in the presence of an optical cavity. Table S1, Supporting Information summarizes experimental results on photon and polariton ASE and lasing in $MAPbBr_3$ and $CsPbBr_3$-based PWs, microwire/nanowire waveguides, vertical microcavities, and metasurfaces at room temperature. To the best of our knowledge, despite the extensive research on lasing/ASE in $MAPbBr_3$ and $CsPbBr_3$, the observation of two distinct lasing thresholds has only been reported in a vertical microcavity.[31] Additionally, as shown in Table S1, Supporting Information, polariton ASE and lasing have been observed even at carrier densities significantly above ρ_M,[8,32] while photon lasing have also been triggered at thresholds well below ρ_M,[4–6,33–36] contrary to the expected transition from exciton-polariton lasing to photon lasing. These puzzling and controversial results underscore the need for a direct experimental approach to clarify the microscopic nature of stimulated emission in these materials.

To this end, we investigated unpatterned $MAPbBr_3$ PWs, motivated by the following considerations. Photon lasing requires the material absorption coefficient, $\alpha(\omega)$, to change into optical gain in the spectral region of stimulated emission. However, measuring photon gain and distinguishing it from polariton gain is challenging and undocumented in $MAPbBr_3$. Unpatterned PWs can play a key role for two main reasons. First, their simple structure allows for tight optical confinement through total internal reflection, which favors strong in-plane exciton-photon coupling.[21,22] Second, PWs enable the measurement of absorption and gain spectra without the optical distortions typically caused by cavities. This is achieved by measuring the optical transmittance and reflectance perpendicular to the plane of the waveguide, which allows photon amplification to be decoupled from polariton amplification along the waveguide plane. The second experimental challenge is to distinguish between stimulated emission of hybrid light-matter excitations (HLMEs), such as exciton-polaritons, and that of photons. In PWs, this can be demonstrated by leveraging the unique physical properties of HLMEs, the only ones that can bleach band-edge absorption due to the interaction of their matter component with the electronic reservoir.[37]

To this aim, we configured a femtosecond spectroscopy station to measure transient transmission and reflection spectra-from which absorption and gain coefficient spectrograms can be determined- and transient photoluminescence spectra. ASE was found to occur in the absence of photon gain and population inversion up to carrier densities $\approx 4{\cdot}10^{19}$ cm^{-3}, far above the Mott density. By comparing the transient kinetics of absorption bleaching and ASE, we established that the latter always involves HLMEs. Since nanopatterning of the PW surface can neither convert the material's optical absorption into gain nor alter the hybrid nature of the stimulated excitations, our experimental results can offer a natural explanation for why two ASE/lasing thresholds have never been observed in any $MAPbBr_3$ photonic structure. We solved Maxwell's equations for the waveguide structure using the measured density-dependent optical permittivity. In agreement with the intriguing experimental observation of stimulated emission of HLMEs in the absence of photon gain and a completely bleached exciton resonance, we found that light-matter interaction in this excitation regime leads to hybrid modes with an energy-wavevector dispersion below the bandgap resembling that of the lower exciton-polariton band. From an application perspective, $MAPbBr_3$ PWs offer ease of fabrication and nano/micropatterning, combined with the exceptional physical properties of hybrid light-matter excitations, such as high nonlinearity, low lasing thresholds, robustness at high carrier densities, and room-temperature operation. They also have the potential to amplify signals over a wide amplification band, with the additional prospect of being electrically modulated[23] and excited.[38]

2. Results and Discussion

2.1. Femtosecond Tandem Spectroscopy Applied to Planar Waveguides

We have investigated perovskite PWs consisting of a methylammonium lead bromide ($MAPbBr_3$) polycrystalline film on a glass substrate with a thin protective overlayer of poly(methyl methacrylate) (PMMA) (see Experimental Section and Figure S1A–C, Supporting Information). Tight light confinement in the waveguide is achieved through total internal reflection. Optical leakage is primarily caused by defects such as surface roughness and irregular film morphology, which lead to scattering (Figure S1D, Supporting Information).[39,40] As a result, diffused photons exiting the waveguide have random directions and carry no useful information about the in-plane wavevector of the waveguide modes prior to scattering.

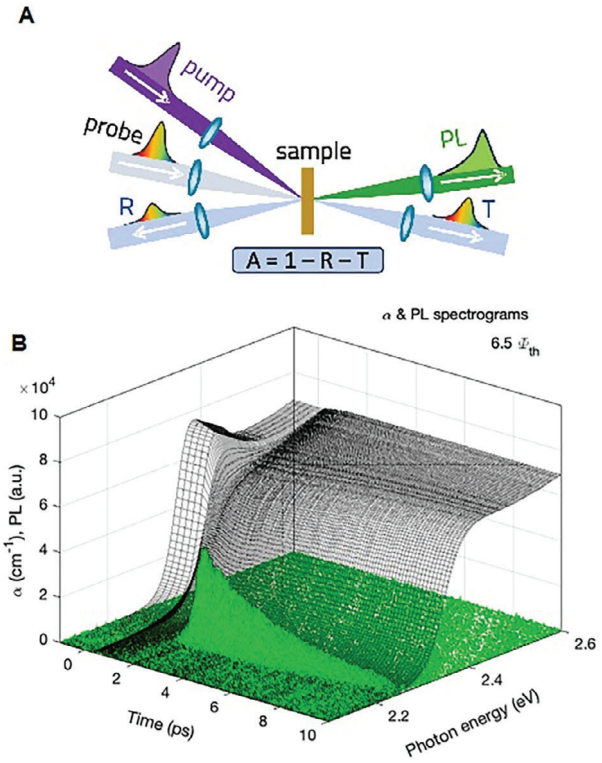

Figure 1. Transient optical absorption and photoluminescence measured by femtosecond tandem spectroscopy. A) Experimental set-up of femtosecond tandem spectroscopy with optical probe at near normal incidence. B) Spectrograms of the perovskite absorption coefficient (α), grey lines, and photoluminescence (PL), green lines, following ultrafast excitation at room temperature (295 K).

We set up a spectroscopic station aimed to measure the spectrograms of the light transmitted and reflected from the same excited spot on the film where the collected photoluminescence (PL) originates (**Figure** 1A). Transmission, reflection, and PL are nonlinearly dependent on the photoexcited carrier density, so it is critical that all three spectroscopies monitor precisely the same carrier density profile. The nonlinearities in the optical response were induced by a nonresonant femtosecond laser excitation. The transmittance (T) and reflectance (R) spectra of weak probe pulses were recorded as a function of time delay so to assess the spectrograms of the film absorptance, $A(\hbar\omega, \Delta t) = 1 - T(\hbar\omega, \Delta t) - R(\hbar\omega, \Delta t)$. Positive values of $A(\hbar\omega, \Delta t)$ mean optical absorption, negative ones indicate optical amplification. Our approach mimics that of continuous wave spectrophotometers but introducing the femtosecond time resolution necessary to study the kinetics of nonlinear light-matter interactions and many-body effects under pulsed excitation. The absorption (gain) coefficient α ($g = -\alpha$) of the material was then estimated from $T(\hbar\omega, \Delta t)$ and $R(\hbar\omega, \Delta t)$ spectrograms with extremely high sensitivity, around a few tens of cm^{-1} (see Note S1 and Figures S2–S5, Supporting Information). Within the same spectroscopic station, we also measured PL spectrograms and accessed the kinetics of the emission transients with an optical-Kerr-gate setup, with femtosecond risetime resolution, or with a 2D streak camera for enhanced sensitivity at the cost of reduced time resolution (50 ps).

When the sample is excited with an excitation pulse fluence above a threshold (Φ_{th}) of 25 μJ cm^{-2}, corresponding to an injected carrier density (ρ_{th}) of $4{\cdot}10^{18}$ cm^{-3}, a nonlinear emission emerges on the low-energy side of the spontaneous emission. This emission, attributed to ASE, becomes progressively more dominant at higher pulse fluences. Representative results of femtosecond tandem spectroscopy in this nonlinear regime, specifically for a pulse fluence of $6.5{\cdot}\Phi_{th}$, are illustrated in Figure 1B, which plots the photoluminescence, PL($\hbar\omega$, Δt), and absorption, $\alpha(\hbar\omega, \Delta t)$, spectrograms. The PL($\hbar\omega$, Δt) signal features a laser-like photon burst peaking at $\Delta t \approx 2$ ps after excitation and lasts a few picoseconds. In contrast, the sub-threshold spontaneous emission, shown in **Figure** 2B, is spectrally broader and has a much longer lifetime, on the order of nanoseconds.[41] The absorption spectrogram shows an initial ultrafast transient lasting ≈1 ps,[42] during which the exciton resonance is fully bleached, leaving mainly the absorption edge of continuum interband transitions with an ultrashort-lived low-energy tail. A more detailed examination of the initial transient absorption bleaching will be provided later in the manuscript. This phase is dominated by carrier thermalization and lattice reorganization, followed by the slower regime of interest for our study, characterized by two key features: (i) no optical gain is observed at any time delay, a phenomenon that will be investigated in more detail in the next paragraph; (ii) the absorption near the exciton resonance shows a transient partial recovery complementary to the decay of the PL burst, suggesting that amplified spontaneous emission involves HLMEs. The correlation between bleaching recovery and stimulated emission decay will be quantitatively discussed in paragraph 2.3.

2.2. Stimulated Emission without Photon Gain and Population Inversion

Absorption and photoluminescence spectra as a function of pulse fluence are presented in Figure 2. Figure 2A displays the absorption spectra, recorded at $\Delta t = 2$ ps, immediately following the initial ultrafast transient due to carrier thermalization. No optical gain is detected, nor at the threshold ρ_{th} nor at excitations 10 times higher (inset of Figure 2A), precluding the possibility of conventional amplified spontaneous emission of photons due to population inversion (Note S2 and Figure S6, Supporting Information) or other photon stimulated emission processes, for example, involving excitons, as the origin of the intense burst emission. Another important observation is that the exciton peak is clearly visible at the threshold density, ρ_{th}, which is about five times the best theoretical estimate of the Mott density. This suggests that the peak may result from many-body electron-hole correlations, manifesting as the Mahan exciton resonance.[43] The persistence of the exciton-like resonance above the theoretical Mott density has already been observed in $MAPbBr_3$.[30] The exciton peak gradually weakens as the excitation fluence increases above ρ_{th}, and eventually disappears at the highest injected carrier densities. However, the absorption strength of the band-to-band transitions does not decrease, contrary to what is expected for a noninteracting electron-hole plasma (Note S2 and Figure S6D, Supporting Information). This provides further evidence of persistent many-body coulomb correlations at injected

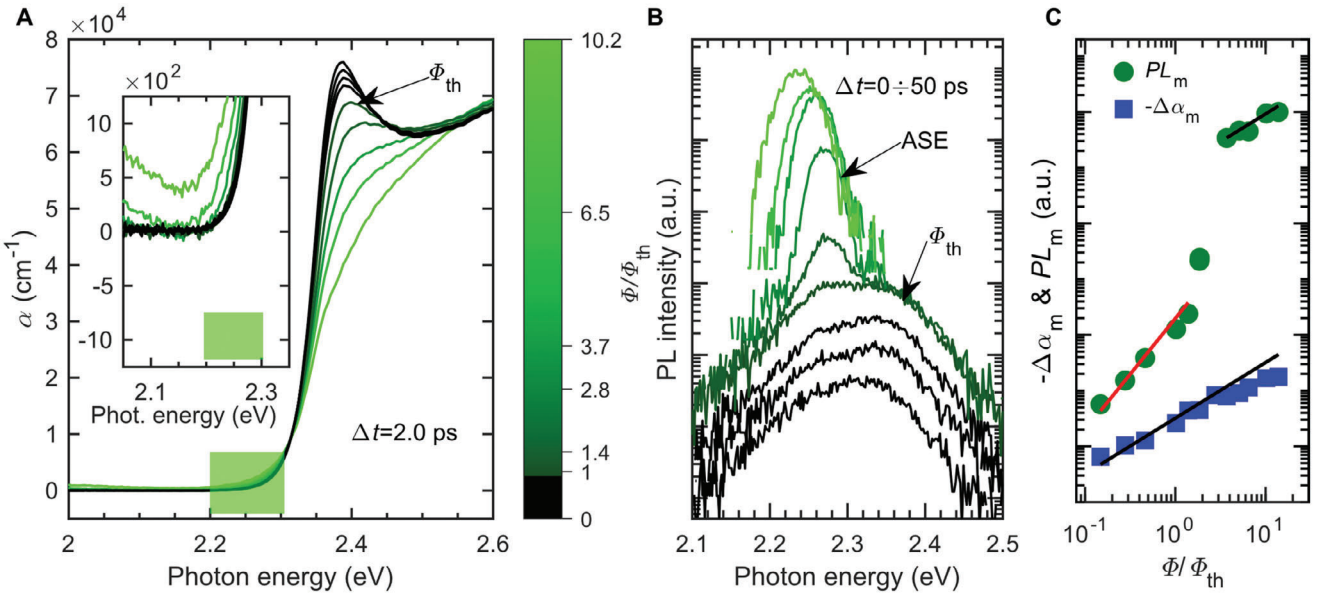

Figure 2. Optical absorption and photoluminescence spectra versus pulse fluence. A) Measured absorption coefficient at $\Delta t = 2.0$ ps as a function of the pulse fluence. Inset: magnification of the absorption spectra in the low energy window. The green rectangles serve as a reference to indicate the spectral region of the observed stimulated emission. B) PL spectra measured by a 2D-streak-camera as a function of excitation fluence in the time window $\Delta t = 0 \div 50$ ps. $\Phi_{th} = 25$ μJ cm^{-2} is threshold pulse fluence above which the narrower amplified spontaneous emission (ASE) band is observed. C) Excitation pulse fluence dependence of maximum values of PL transients (PL_m), in green circles, and differential absorption coefficient ($-\Delta\alpha_m$) spectrally integrated and measured at time delay $\Delta t = 2$ ps, where it reaches the maximum intensity, in blue squares. Continuous black and red lines represent a guide to the eye for linear and quadratic dependence, respectively.

carrier densities up to $4{\cdot}10^{19}$ cm^{-3}, that is, highlighting the inadequacy of non-interacting electron-hole plasma model, which underpins the Mott transition model, in explaining the observed nonlinear optical properties of the electronic reservoir in the stimulated emission regime. Strong electron-hole correlations above the Mott transition are expected to be a general characteristic, with basic theoretical implications and potential application interest. Similar observations have been reported in Ge[44] and Si,[45,46] where the 1s-2p exciton transition was monitored using THz spectroscopy.

Figure 2B shows the PL spectra in the time window $\Delta t = 0 \div 50$ ps, measured at various pulse fluence using a streak-camera. As the excitation fluence increases, the intensity of the spectrally broad spontaneous emission also increases, until the pulse fluence reaches the threshold Φ_{th}. Above this threshold, the intensity of the broad PL saturates, while a narrower ASE band is observed. The ASE contribution, corresponding to the burst emission shown in Figure 1B, becomes dominant at the highest fluences, redshifting and broadening. The redshift runs contrary to expectation for standard photon lasing, where quantum degeneracy is expected to cause a blueshift, the so-called Moss-Burstein effect. Similar phenomenology was observed in $MAPbBr_3$ metasurfaces,[8] $CsPbBr_3$ thin films[7,47] and nanowires.[36] In metasurfaces, nonlinear emission was discussed in terms of stimulated emissions of exciton-polaritons. In nanowires, lasing was attributed to the stimulated emission of a nondegenerate electron-hole plasma involving plasmon emission, with the red shift explained by the dependence of plasmon energy on carrier density.[36,48] In Figure 2B is also shown that the intensity of the spontaneous emission saturates above Φ_{th}, indicating that the majority of photoexcited electron-hole pairs in excess of the threshold density contribute to the ultrafast emission.

Figure 2C reports the maximum intensity of the PL transients (PL_m) as a function of excitation fluence. Figure 2B,C clearly demonstrate that there is only one stimulated emission threshold Φ_{th}. Below Φ_{th}, PL_m scales quadratically with pulse fluence down to the minimum investigated carrier density, $\rho = 6{\cdot}10^{17}$ cm^{-3}, which is approximately equal to the Mott density. Above ρ_M, all excitons are expected to be ionized, implying that spontaneous photon emission can only result from a bimolecular process involving the majority population of unbound electron and hole carriers, which is consistent with the quadratic dependence of PL_m on pulse fluence.[41,49] Above the fluence threshold PL_m exhibits a sharp increase, followed by a linear dependence on Φ, indicating that most of the photoexcitations contribute to the ultrafast photon burst at the highest excitation levels. For comparison, the maximum absolute variation in α, denoted as $|\Delta\alpha_m|$, measured at a time delay of $\Delta t = 2$ ps, is also presented in Figure 2C. $|\Delta\alpha_m|$ is spectrally integrated to exclusively probe optical bleaching, thereby avoiding complexities arising from dispersive many-body effects, such as line broadening and red/blue shifts in electronic transitions, which provide no spectrally integrated contribution.[37,50] $|\Delta\alpha_m|$ exhibits a linear increase as a function of the injected electron-hole pair density, with only a slight saturation observed at the highest excitation levels. This experimental finding demonstrates that $|\Delta\alpha|$, being proportional to the photoexcited carrier density across all the reported excitation fluences, is a reliable indicator of the carrier density, ρ.

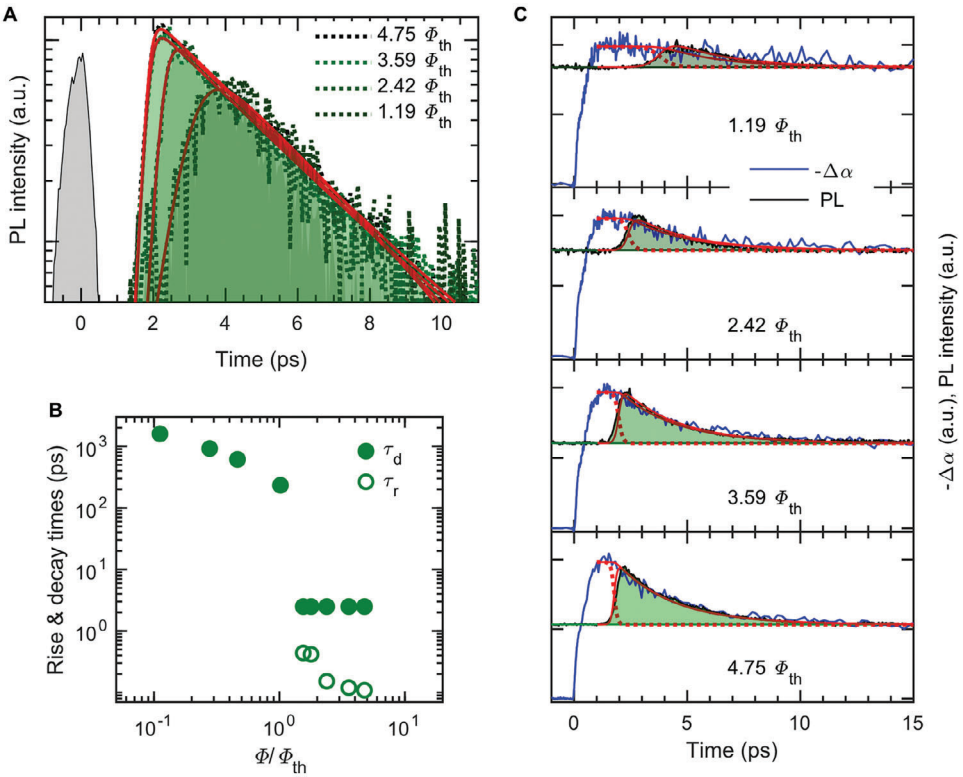

Figure 3. Kinetics of emission burst versus kinetics of absorption bleaching. A) Dashed green lines are the transients of the light burst emitted above threshold fluence at room temperature. All transients were fitted using an asymmetric hyperbolic secant function $[\exp(t/\tau_d) + \exp(-t/\tau_r)]^{-1}$ (solid red lines), with independent τ_r and τ_d. Decay time is independent of pulse fluence, while risetime is below 1 ps and shortens for increasing pulse fluence. The black curve centered at $\Delta t = 0$ ps is the time resolved scattered light of the 100-fs-laser pulses, measured through the optical-Kerr-gate PL setup. The profiles at 4.75 Φ_{th} and 3.59 Φ_{th} are nearly overlapped. However, they can be distinguished by the slight difference between the fitting curves. B) Excitation pulse fluence dependence of τ_d and τ_r. C) $-\Delta\alpha$ transients (continuous blue lines) and PL intensity transients (continuous black lines with filled underline areas) as a function of time for four pulse fluences above Φ_{th}. $\Delta\alpha$ is the spectrally integrated differential absorption coefficient. PL intensity traces were rescaled to fit the initial, fast transients of $-\Delta\alpha$. Dashed red curves represent $-\Delta\alpha$ transients simulated according to the stimulated photon emission model (Equations (1) and (2), b = 0, $k_s = 1.69 \cdot 10^{-4}$ ps^{-1}) while continuous red curves represent $-\Delta\alpha$ and PL transients simulated according to the stimulated HLME emission model (Equations (1) and (2), b = 1.02, $k_s = 1.69 \cdot 10^{-4}$ ps^{-1}).

2.3. Kinetics of Emission Burst versus Kinetics of Absorption Bleaching

We now provide direct experimental evidence that the ultrashort photon emission above threshold stems from the outcoupling of a hybrid light-matter wave propagating along the planar waveguide. We leverage the properties of electrons and holes to induce bleaching of the optical transitions, specifically of the exciton resonance, irrespective of whether electrons and holes are part of the thermal reservoir, in the form of bound or unbound pairs, or strongly coupled with photons to form hybrid quasiparticles.[37,50] By contrasting the PL kinetics with the kinetics of $|\Delta\alpha|$, we demonstrate that only light-matter states can be the final states of the stimulated emission process. **Figure** 3A reports the PL transients at four excitation levels above threshold, detected through an optical Kerr gate to maximize the temporal resolution. The emission burst grows and decays exponentially with rise and decay times τ_r and τ_d, respectively. The PL signal is rescaled to show that, at all excitation fluences above threshold, the intensity decays with the same characteristic time $\tau_d = (2.5 \pm 0.1)$ ps, as highlighted in Figure 3B where rise time and decay time are represented as a function of fluence. Figure 3B also shows that the rise time quickly decreases for growing excitation fluences and reaches the resolution time of the TRPL setup.

Above the threshold fluence, the differential absorption $|\Delta\alpha|$ undergoes a rapid initial decay, associated with the process of stimulated emission. At low pulse fluences, the rate of the stimulated emission is slow enough to allow almost complete energy/lattice relaxation of the hot photoexcited carriers. However, with increasing pulse fluence, the rate becomes so fast that the stimulated scattering begins to compete with the process of hot carrier thermal relaxation. This could possibly explain why population inversion is never observed, even shortly after excitation.

Figure 3C shows a quantitative comparison between the transient PL emission and $|\Delta\alpha|$. For this purpose, the PL traces have been rescaled, and their baselines have been aligned with the slow decay component of $|\Delta\alpha|$. The key observation is that the decay of the PL intensity corresponds to the initial decay of $|\Delta\alpha|$, that is, to the decay of the injected electron-hole population, as expected only if stimulated emission involves hybrid light-matter quasiparticles and not pure photons. We have simulated the process of stimulated emission by empirical rate equations for the

overall nonequilibrium hybrid light-matter/photon populations and reservoir photoexcitations in the probed excited sample spot. The rate equations account for all the processes that can deplete or increase the excess reservoir population that undergoes stimulated emission (Δn_r) and the nonequilibrium population (n_p) accumulating in hybrid light-matter/photon states emerging from stimulated scattering:

$$\Delta \dot{n}_r = -k_s \left(n_p + 1\right) \Delta n_r - k_r \Delta n_r \quad (1)$$

$$\dot{n}_p = +k_s \left(n_p + 1\right) \Delta n_r - k_p n_p \quad (2)$$

The second terms in Equation (1) and (2) represent the spontaneous decay rates of HLME/photons inside the slab and the reservoir populations, respectively. Given that $k_r = 1\ \mathrm{ns}^{-1}$ is very small, its exact value is irrelevant for the ultrafast stimulated emission kinetics. The value of $k_p = 1/2.5\ \mathrm{ps}^{-1}$ is taken from the experiment. The first terms in Equation (1) and (2) account for the stimulated boson scattering from the reservoir population to the nonequilibrium population in hybrid light-matter/photon states. The PL signal is proportional to n_p, either in the case of photon or hybrid populations. $|\Delta\alpha|$ is proportional to $\Delta n_r + b n_p$, where b is the bleaching strength of the hybrid/photon population relative to that of the reservoir excitations. In the case of photon amplification, $b = 0$. The initial conditions were set as follows: $n_p(0) = 0$, while $\Delta n_r(0) = 6{\cdot}10^4$ for $\Phi = 3.59 \cdot \Phi_{th}$ (Note S3, Supporting Information). We determined the start of the stimulated emission to coincide with the end of the ultrafast relaxation and thermalization process, $\Delta t = 1$ ps. For other levels of carrier injection, $\Delta n_r(0)$ was rescaled according to the effective pulse fluence. A global least-squares fit to all $|\Delta\alpha|$ and PL transients gave $b = 1.02 \pm 0.02$, a value that fully confirms the hybrid light-matter nature of the final state of the stimulated emission process. The result $b \approx 1$ means that the bleaching power of the nonequilibrium HLME population is equal to that of thermal excitations from which they are scattered, which is not surprising. On one hand, hybrid quasiparticles are likely to have a lower bleaching efficiency, which is due to their matter component only. On the other hand, this can be largely compensated by the fact that they represent a non-equilibrium population with small wavevectors. In fact, according to many-body theories, this non-equilibrium population is expected to bleach the exciton resonance more efficiently than a thermal reservoir population, which is distributed over a much larger momentum space volume due to the much heavier mass of both electrons and holes.[50] The photon simulations ($b = 0$, red dashed curves in Figure 3C) are also presented, and, as expected, they completely fail to replicate the experimental results. In this scenario, $|\Delta\alpha|$ decays with a time constant equal to the rise time of the PL signal.

Finally, superfluorescence from a coherent exciton population has recently been observed in $MAPbI_3$[51] and $CsPbBr_3$[52] thin films. However, interpreting the nonlinear emission we observed in $MAPbBr_3$ PWs as superfluorescence is inconsistent with the following observations. (i) A non-degenerate electron-hole plasma, rather than excitons, constitutes the majority of thermal photoexcitations.[41,49] (ii) The nonlinear emission is observed well above the Mott transition and at carrier densities where the exciton resonance is completely bleached. (iii) The nonlinear emission redshifts and broadens with increasing pulse fluence, a phenomenology that is difficult to explain in terms of exciton superfluorescence. In contrast, this behavior is naturally explained by HLMEs, assuming that stimulated scattering from the nondegenerate electron-hole plasma into HLMEs involves plasmon emission, whose energy increases with plasma density.[36] (iv) We attempted to fit the PL transients under the assumption of superfluorescence; however, this analysis failed to accurately reproduce the temporal behavior, particularly the rise time and delay of the burst emission as a function of pulse fluence, as discussed in Note S3, Supporting Information.

We also investigated stimulated emission at 180 K to ensure a more pronounced excitonic resonance and to favor the achievement of population inversion, and thus photon gain. Experimental results confirm i) that stimulated emission involves HLMEs in the absence of photon gain and population inversion; ii) the persistence of the exciton resonance is observed at all achievable photoexcitation densities, far above the Mott density (Figures S7–S9, Supporting Information).

2.4. Hybrid-Light Matter Excitations above Threshold: A Parameter-Free Numerical Simulation

Tandem spectroscopy demonstrates that the burst emission observed in PL spectrograms in $MAPbBr_3$ waveguides results from stimulated scattering of hybrid light-matter quasiparticles from a thermal electronic reservoir. In vertical microcavities, hybrid light-matter modes are always associated to exciton-polaritons. However, in our experiments the measurement of the absorption spectrum proves that the stimulated population still maintains its hybrid nature even though the exciton peak is strongly suppressed and eventually disappears at the highest fluences.

Complementary numerical approaches (Note S4 and Figures S10–S13; Note S5 and Figures S14 and S15, Supporting Information) have been used to calculate the HLME dispersion in the actual waveguide structure shown in **Figure 4A**. Figure 4C reports the absorption spectrum of $MAPbBr_3$ thin films. The contribution of the exciton resonance is distinguishable, but the electron-hole binding energy is not large enough to isolate it from the continuum of interband transitions, even at low temperatures (see Figure S7, Supporting Information). To avoid any a priori assumptions about which electronic states are strongly coupled to photons and the relative coupling strength, the measured complex permittivity must be used. This measurement is typically performed on unexcited devices, where the material permittivity is determined through linear optical experiments.[10] However, our experimental approach allows for estimating the complex permittivity at any carrier density, as detailed in Note S4 and Figure S11, Supporting Information. This capability enables us to solve Maxwell's equations above the stimulated emission threshold without approximations, such as the single Lorentz oscillator (LO) model for the exciton resonance or a constant refractive index, which are commonly used for estimating exciton-polariton or photon dispersion, respectively.[22,53,54]

Figure 4B shows the field intensity distribution of the fundamental transverse-electric (TE_0) waveguide eigenmode, that is, the solution of Maxwell's equations for a given (real) propagation constant, β, in the case of $MAPbBr_3$ on glass substrate. The

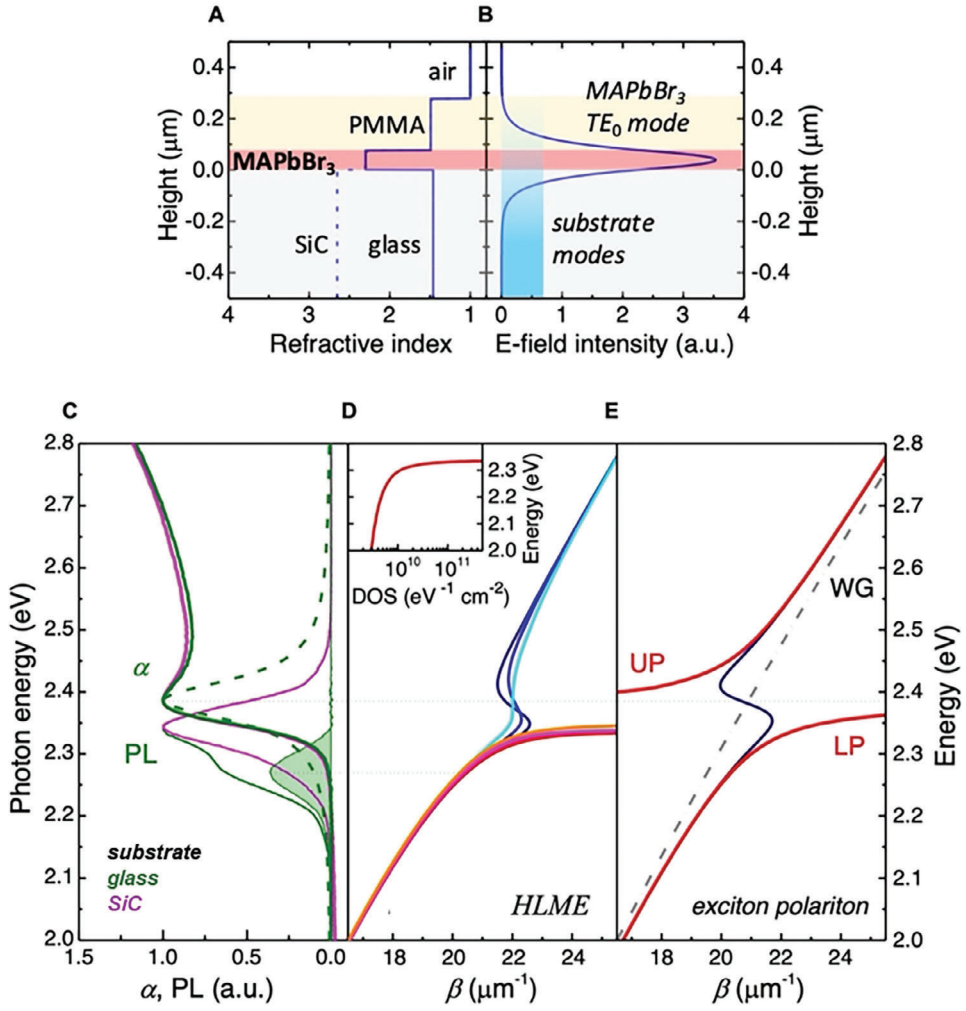

Figure 4. HLME versus exciton-polariton in perovskite planar waveguides. A) Spatial profile of the real refractive index of the layers composing the perovskite planar waveguide. B) Spatial profile of the perovskite-confined TE_0 mode in the case of glass substrate, with shaded blue region representing a continuous distribution of substrate-confined modes. C) Normalized absorption coefficient (α), and photoluminescence (PL), measured at room temperature in the linear absorption regime, well below threshold, in the case of $MAPbBr_3$ on glass (green) or SiC (magenta) substrate. The curve with filled area is the HLME radiative leakage due to scattering by waveguide imperfections. The dashed green line is the absorption spectrum of a Lorentz oscillator describing a homogeneously broadened exciton resonance in $MAPbBr_3$ in the absence of continuum interband transitions. D) Dispersion for HLME eigenmodes (red, magenta and orange) and for driven modes (dark blue, blue and cyan) in the waveguide on glass, calculated using the measured optical permittivity of the perovskite ($<\Phi_{th}$, Φ_{th} , $6.5\cdot\Phi_{th}$). The inset shows the HLME density of states versus energy in linear absorption regime. (E) TE_0 waveguide exciton-polariton dispersion estimated with the LO model, with lower polariton (LP) and upper polariton (UP) eigenmodes (red lines) and LO driven modes (blue line). The dash-dotted line is the dispersion of the bare waveguide (WG) TE_0 mode, as estimated from the background dielectric function of $MAPbBr_3$.

fundamental TE_0 mode, evaluated at threshold excitation fluence and at the polariton energy of 2.284 eV, is characterized by a confinement factor of 54% and an effective refractive index n_{eff} = 1.793+0.003i. Below the perovskite absorption edge, the HLME dispersion is similar to that expected for the lower exciton-polariton (LP) band (Figure 4D). For energies above the exciton resonance, the absorption from the electron-hole continuum leads instead to a broad distribution of overdamped eigenmodes, while the dispersion of the driven modes, that is, the solutions of the Maxwell's equations for a driving (real) frequency, deviates only slightly from that of the bare waveguide modes. Contrasting HLME dispersion calculated using the measured complex permittivity with that using a single Lorentz oscillator to model the exciton resonance is useful for highlighting the inherent contribution of continuum states. For a quantitative comparison, the LO peak absorption coefficient, spectral linewidth and background optical permittivity were adjusted to those of the perovskite excitonic resonance (see Figure 4C). As expected, the LO model leads to the recovery of a well-defined upper polariton (UP) band in the waveguide eigenmode dispersion. Accordingly, the driven modes exhibit an antisymmetric S-shaped dispersion around the exciton-waveguide mode crossing point (see Figure 4E). Finally, the effect of the strong coupling between the sole exciton resonance and the bare waveguide mode on the LP band is slightly reduced as compared to the case where continuum interband transitions are included (Figure 4D,E).

The contribution of hybrid states to the waveguide PL spectrum at low excitation levels was evaluated by comparing the PL spectrum of PMMA/$MAPbBr_3$/glass waveguides with that of PMMA/$MAPbBr_3$/SiC structures, which do not support guided modes (Figure 4A–C). PL from the PMMA/$MAPbBr_3$/glass waveguides features a low-energy shoulder, which is missing in the PMMA/$MAPbBr_3$/SiC samples. We attribute this low-energy emission to radiative leakage of hybrid light-matter states caused by waveguide defects such as surface roughness and irregular film morphology.[39,40] Statistics on several samples confirm that the intensity of the PL shoulder depends on film morphology (Figure S16, Supporting Information). Conversely, emission from hybrid light-matter states was never observed in PMMA/$MAPbBr_3$/SiC samples. Emission from HLMEs in glass-based waveguides is found to occur at values of the propagation constant just below the crossing point between the exciton resonance and the bare waveguide mode (Figure 4D), where HLMEs have an ultralight ($< 10^{-5}\ m_e$) and negative effective mass, leading to a density of states lower than $10^{10}\ eV^{-1}\ cm^{-2}$ and a group velocity of $(7 \pm 1)\cdot 10^7\ m\ s^{-1}$. In PMMA/MAPbBr3/SiC samples, no emission was observed, confirming the absence of guided electromagnetic waves as predicted by simulations.

We extended eigenmode and driven mode analyses using the measured optical permittivity at the highest excitation levels. Both solutions exhibit stable LP-like dispersion across all excitation levels (Figure 4D). Figures S12 and S13, Supporting Information show that the HLME dispersion at high carrier densities, calculated using the measured optical permittivity, can be approximately replicated using a single LO-based optical permittivity, but only assuming an unrealistic, density independent, oscillator strength (Figures S11 and S12, Supporting Information). This analysis demonstrates that the robustness of HLMEs in perovskite planar waveguides arises from the electronic polarization induced by all bandgap transitions. The strength of the overall electronic polarization contribution to the hybrid waves is only weakly reduced as the excitation density exceeds the Mott density due to many-body electron-hole correlations.[30]

To the best of our knowledge, two lasing thresholds were observed in two experiments involving $CsPbBr_3$ and $CsPbCl_3$ vertical microcavities, cavity geometry also known as Vertical Cavity Surface Emitting Laser (VCSEL).[31,55] A careful investigation of the emission direction in $CsPbCl_3$ vertical microcavities showed that this changed from vertical (surface emitter) to horizontal (edge emitter), below and above the second threshold, respectively.[55] The vertical coherent emission below the second threshold was interpreted as polariton lasing, while the horizontal emission above the second threshold was attributed to photon lasing. However, this latter interpretation contrasts with the expectation that the direction of photon lasing in VCSELs should be vertical. Instead, this unusual behavior is consistent with in-plane stimulated emission of HLMEs.

3. Conclusion

In this work, we have studied the microscopic mechanisms of stimulated emission in metal halide perovskites, a process widely explored but not yet fully understood. Controversial results reported in literature are mostly based on the investigation of angle-resolved photoluminescence in laser cavities. Our experimental strategy was focused instead on two fundamental features that distinguish stimulated emission: (i) whether the materials develop photon gain, in the absence of which no photon lasing can occur, and (ii) whether the stimulated excitations have an electronic component, without relying on their energy-wavevector dispersion, which is difficult to measure above the lasing threshold. We addressed the first point by measuring the density-dependent absorption and gain transient spectra in $MAPbBr_3$ planar waveguides. The second challenge was addressed by monitoring the bleaching of the absorption spectrum, which can be induced only by the matter component of the hybrid excitations.

We have shown that amplified spontaneous emission in $MAPbBr_3$ planar waveguides results from a single microscopic mechanism that involves stimulated scattering of hybrid light-matter excitations at all carrier densities above the threshold, even when the exciton resonance disappears, and it always occurs without photon gain. A second threshold, possibly indicating a transition of stimulated emission from hybrid light-matter excitations to bare photons, was never observed.

To verify that planar waveguides can support hybrid light-matter excitations even in the excitation regime where the exciton resonance is strongly bleached or absent, we solved Maxwell's equations for the waveguide structure across all carrier densities, without relying on free parameters or making any a priori assumption. This was made possible because our experimental approach allowed us to measure the material optical permittivity as a function of the carrier density. Numerical solutions confirm that, contrary to common belief, the experimentally observed steep absorption edge, in the absence of an exciton resonance, leads to propagating light-matter modes. These modes exhibit a linear photon-like dispersion at low wavevectors, lack an energy minimum, and demonstrate an anti-crossing behavior approaching the bandgap energy at higher wavevectors.

The potential of femtosecond tandem spectroscopy to unravel the microscopic nature of stimulated emission processes can be extended to other 3D or 2D hybrid perovskites. A comprehensive understanding of light-matter interactions in the whole class of metal halide perovskites is foundational for advanced device engineering through surface patterning, electrical modulation and injection capabilities,[38] and seamless integration within on-chip photonic circuits.

4. Experimental Section

Waveguide Fabrication: Thin films of $MAPbBr_3$ were fabricated on top of soda-lime glass slides and SiC wafers by spin coating technique inside a nitrogen-filled glove box. The precursor solution were obtained by dissolving MABr (99.99% Greatcell Solar) and $Pb(CH_3CO_2)_2 \cdot 3H_2O$ (99.99% Merk) in dimethylformamide (DMF, 99.8% Merk) with molar ratio 3:1 and 0.5 M final concentration. Two drops of solution were spun on the substrates at 6000 rpm for 60 s. After solution deposition, the samples were annealed at 100° for 10 min. A thin film of PMMA was then deposited on $MAPbBr_3$ films as protective layer with a 35 mg/ml PMMA solution in chlorobenzene.

Waveguide Characterization: Optical reflectance/transmittance spectra of thin films were recorded using a dual-beam spectrophotometer (Agilent Technologies Cary 5000 UV–vis-NIR) with integrating sphere accessory. Film thickness was determined by measuring the step height of a blade scratch in the sample with atomic-force microscopy (AFM) using NT_MDT Solver P47H-Pro in semicontact mode. $MAPbBr_3$ films on glass and on SiC were characterized by X-ray diffraction (XRD) and AFM before

PMMA coating. Room-temperature XRD patterns showed the perovskite cubic lattice with space group $Pm\bar{3}m$, and no degradation was detected. The root-mean square (RMS) roughness calculated from AFM was similar in both sample types, namely 11.6 nm in $MAPbBr_3$/glass and 8.8 nm in $MAPbBr_3$/SiC (see Figure S1, Supporting Information).

Spectroscopic Station: A home-made spectroscopic station was setup to acquire the linear reflectance/transmittance spectra, the differential reflectance/transmittance spectrograms, and the photoluminescence spectrograms (see Note S2 and Figures S2–S5 and S7–S9, Supporting Information). All measurements were taken on the same excited sample spots, inside a transient absorption spectrometer (Ultrafast Systems Helios) at various lattice temperatures and excitation pulse fluences. The spectral response function of the transient absorption spectrometer was calibrated by reference measurements taken in the dual-beam spectrophotometer. For low-temperature measurements, the sample was kept inside a cryostat (Janis ST-500). The primary laser source was a titanium:sapphire regenerative amplifier (Coherent Libra), delivering a 1 kHz train of 100-fs long pulses at 794 nm wavelength. Output pulses were sent to an optical parametric amplifier (Topas 800 from Light Conversion) to generate laser pulses at shorter wavelengths to excite the samples. In time-resolved nonlinear absorption spectroscopy the linear reflectance/transmittance spectra and differential reflectance/transmittance spectrograms were combined to yield nonlinear spectrograms for the perovskite absorption/gain coefficient at various lattice temperatures and excitation pulse fluences. To measure the time-resolved photoluminescence spectrograms, the light emitted perpendicularly to the waveguide was sent either to either a 2D streak camera (Hamamatsu C10910), coupled to a grating spectrometer (Princeton Instruments Acton SpectraPro 2300i), with 50-ps time resolution; or to an Optical-Kerr-gated photoluminescence setup with subpicosecond resolution, using a 1-mm-thick quartz plate as gating medium, a 794-nm beam from the regenerative amplifier as the gating beam and employing nanoparticle linear film polarizers (LPVISA from Thorlabs). Kerr-gated PL was detected through a grating spectrometer (Acton SpectraPro 2300i) with a CCD detector (Andor Newton) using home-made software. The conversion efficiency for gates PL was over 6%, with typical rise-time temporal resolution of ≈100 fs.

Supporting Information

Supporting Information is available from the Wiley Online Library or from the author.

Acknowledgements

All authors acknowledge CeSAR—Centro Servizi di Ateneo per la Ricerca—at the Università degli Studi di Cagliari. All authors thank Dr. M. Marceddu and Dr. E. Podda for technical assistance. E.D.C., P.P., and F.Q. acknowledge INFN Cagliari for access to Ansys/Lumerical License. This work was funded by Fondazione di Sardegna through project 2F20000210007 "Perovskite materials for photovoltaics" (F.Q.) and project F73C22001160007 "Single crystal hybrid perovskite thin films for optoelectronics" (D.M., G.B., M.S., A.M.). This work was supported by Associazione Università Sulcis Iglesiente (AUSI), delibera CTS del 05-03-2019 e rinnovi successivi (A.M., G.B., F.Q., M.S., D.M.) A.S. was supported by PON R&I "Ricerca e Innovazione" 2014–2020 CCI2014IT16M2OP005 Azione IV.4. Contratti di ricerca su tematiche Green – CUP F35F21002390008. This study was developed in the framework of the research activities carried out within the Project "Network 4 Energy Sustainable Transition—NEST," Spoke 1., Project code PE0000021, funded under the National Recovery Hence Plan (NRRP), Mission 4, Component 2, Investment 1.3— Call for tender No. 1561 of 11.10.2022 of Ministero dell'Universita' e della Ricerca (MUR); funded by the European Union—NextGenerationEU (M.S., D.M., V.D.); Ecosystem of Innovation for Next Generation Sardinia, Spoke 7 – Project code ECS00000038, Low carbon technologies (A.M.). This work was funded by MUR through PRIN 2022 grants: 2022HWWW3S – INTERFACE (F.Q.), 2022F2K7J5 – MIRROR (R.P., F.P., A.M.), 2022EHER2H – ISoTOPe (R.P., D.M.), 2022XP37C7 – Newatomist (G.B.), 2022YM3232 – NanoPix (M.S.), and through PRIN 2022 PNRR grants: P2022ZYTJY – Master (A.S., M.S.), P20224PJJN – Orienting (G.B., A.M., D.M.), P2022W9773 – DELPHI (F.P., F.Q.).

Open access publishing facilitated by Universita degli Studi di Cagliari, as part of the Wiley - CRUI-CARE agreement.

Conflict of Interest

The authors declare no conflict of interest.

Author Contributions

A.S. and F.P. contributed equally to this work. Manuscript was written by A.S., M.S., F.Q., G.B. and the final version was revised and approved by all the authors.

Data Availability Statement

The data that support the findings of this study are available from the corresponding author upon reasonable request.

Keywords

amplified spontaneous emission, hybrid perovskites, polariton gain, waveguides

Received: October 17, 2024
Revised: November 26, 2024
Published online:

[1] F. Zhao, A. Ren, P. Li, Y. Li, J. Wu, Z. M. Wang, *ACS Nano* **2022**, *16*, 7116.
[2] Q. Zhang, Q. Shang, R. Su, T. T. H. Do, Q. Xiong, *Nano Lett.* **2021**, *21*, 1903.
[3] A. Karabchevsky, *Light Sci. Appl.* **2023**, *12*, 160.
[4] N. Pourdavoud, A. Mayer, M. Buchmüller, K. Brinkmann, T. Häger, T. Hu, R. Heiderhoff, I. Shutsko, P. Görrn, Y. Chen, H.-C. Scheer, T. Riedl, *Adv. Mater. Technol.* **2018**, *3*, 1.
[5] N. Pourdavoud, T. Haeger, A. Mayer, P. J. Cegielski, A. L. Giesecke, R. Heiderhoff, S. Olthof, S. Zaefferer, I. Shutsko, A. Henkel, D. Becker-Koch, M. Stein, M. Cehovski, O. Charfi, H.-H. Johannes, D. Rogalla, M. C. Lemme, M. Koch, Y. Vaynzof, K. Meerholz, W. Kowalsky, H.-C. Scheer, P. Görrn, T. Riedl, *Adv. Mater.* **2019**, *31*.
[6] C. Huang, C. Zhang, S. Xiao, Y. Wang, Y. Fan, Y. Liu, N. Zhang, G. Qu, H. Ji, J. Han, L. Ge, Y. Kivshar, Q. Song, *Science* **2020**, *367*, 1018.
[7] A. Palatnik, C. Cho, C. Zhang, M. Sudzius, M. Kroll, S. Meister, K. Leo, *Adv. Photonics Res.* **2021**, *2*, 2100177.
[8] M. A. Masharin, A. K. Samusev, A. A. Bogdanov, I. V. Iorsh, H. V. Demir, S. V. Makarov, *Adv. Funct. Mater.* **2023**, *33*, 2215007.
[9] C. Chang, Y. Shi, C. Zou, L. Y. Lin, *Adv. Photonics Res.* **2023**, *4*, 2200071.
[10] X. Wu, S. Zhang, J. Song, X. Deng, W. Du, X. Zeng, Y. Zhang, Z. Zhang, Y. Chen, Y. Wang, C. Jiang, Y. Zhong, B. Wu, Z. Zhu, Y. Liang, Q. Zhang, Q. Xiong, X. Liu, *Nat. Commun.* **2024**, *15*, 3345.
[11] P. G. Savvidis, J. J. Baumberg, R. M. Stevenson, M. S. Skolnick, D. M. Whittaker, J. S. Roberts, *Phys. Rev. Lett.* **2000**, *84*, 1547.
[12] M. Saba, C. Ciuti, J. Bloch, V. Thierry-Mieg, R. André, L. S. Dang, S. Kundermann, A. Mura, G. Bongiovanni, J. L. Staehli, B. Deveaud, *Nature* **2001**, *414*, 731.

[13] H. Deng, G. Weihs, C. Santori, J. Bloch, Y. Yamamoto, *Science* **2002**, *298*, 199.
[14] J. Kasprzak, M. Richard, S. Kundermann, A. Baas, P. Jeambrun, J. M. J. Keeling, F. M. Marchetti, M. H. Szymanska, R. André, J. L. Staehli, V. Savona, P. B. Littlewood, B. Deveaud, L. S. Dang, *Nature* **2006**, *443*, 409.
[15] R. Balili, V. Hartwell, D. Snoke, L. Pfeiffer, K. West, *Science* **2007**, *316*, 1007.
[16] T. Byrnes, N. Y. Kim, Y. Yamamoto, *Nat. Phys.* **2014**, *10*, 803.
[17] S. Kéna-Cohen, S. R. Forrest, *Nat. Photonics* **2010**, *4*, 371.
[18] D. Sanvitto, S. Kéna-Cohen, *Nat. Mater.* **2016**, *15*, 1061.
[19] R. Su, A. Fieramosca, Q. Zhang, H. S. Nguyen, E. Deleporte, Z. Chen, D. Sanvitto, T. C. H. Liew, Q. Xiong, *Nat. Mater.* **2021**, *20*, 1315.
[20] M. D. Fraser, S. Höfling, Y. Yamamoto, *Nat. Mater.* **2016**, *15*, 1049.
[21] P. M. Walker, L. Tinkler, M. Durska, D. M. Whittaker, I. J. Luxmoore, B. Royall, D. N. Krizhanovskii, M. S. Skolnick, I. Farrer, D. A. Ritchie, *Appl. Phys. Lett.* **2013**, *102*, 012109.
[22] A. Canales, D. G. Baranov, T. J. Antosiewicz, T. Shegai, *J. Chem. Phys.* **2021**, *154*, 024701.
[23] I. Rosenberg, Y. Mazuz-Harpaz, R. Rapaport, K. West, L. Pfeiffer, *Phys. Rev. B* **2016**, *93*, 1.
[24] T. Ellenbogen, K. B. Crozier, *Phys. Rev. B: Condens. Matter* **2011**, *84*, 3.
[25] J. Ciers, J. G. Roch, J.-F. Carlin, G. Jacopin, R. Butté, N. Grandjean, *Phys. Rev. Appl.* **2017**, *7*, 1.
[26] F. Hu, Y. Luan, M. E. Scott, J. Yan, D. G. Mandrus, X. Xu, Z. Fei, *Nat. Photonics* **2017**, *11*, 356.
[27] O. Jamadi, F. Reveret, P. Disseix, F. Medard, J. Leymarie, A. Moreau, D. Solnyshkov, C. Deparis, M. Leroux, E. Cambril, S. Bouchoule, J. Zuniga-Perez, G. Malpuech, *Light Sci. Appl.* **2018**, *7*, 82.
[28] N. F. Mott, *Rev. Mod. Phys.* **1968**, *40*, 677.
[29] H. Deng, G. Weihs, D. Snoke, J. Bloch, Y. Yamamoto, *Proc. Natl. Acad. Sci.* **2003**, *100*, 15318.
[30] T. Palmieri, E. Baldini, A. Steinhoff, A. Akrap, M. Kollár, E. Horváth, L. Forró, F. Jahnke, M. Chergui, *Nat. Commun.* **2020**, *11*, 850.
[31] J. Feng, J. Wang, A. Fieramosca, R. Bao, J. Zhao, R. Su, Y. Peng, T. C. H. Liew, D. Sanvitto, Q. Xiong, *Sci. Adv.* **2021**, *7*, eabj6627.
[32] T. J. S. Evans, A. Schlaus, Y. Fu, X. Zhong, T. L. Atallah, M. S. Spencer, L. E. Brus, S. Jin, X.-Y. Zhu, *Adv. Opt. Mater.* **2018**, *6*.
[33] H. Zhu, Y. Fu, F. Meng, X. Wu, Z. Gong, Q. Ding, M. V. Gustafsson, M. T. Trinh, S. Jin, X.-Y. Zhu, *Nat. Mater.* **2015**, *14*, 636.
[34] S. W. Eaton, M. Lai, N. A. Gibson, A. B. Wong, L. Dou, J. Ma, L.-W. Wang, S. R. Leone, P. Yang, *Proc. Natl. Acad. Sci. U. S. A.* **2016**, *113*, 1993.
[35] J. Feng, X. Yan, Y. Zhang, X. Wang, Y. Wu, B. Su, H. Fu, L. Jiang, *Adv. Mater.* **2016**, *28*, 3732.
[36] A. P. Schlaus, M. S. Spencer, K. Miyata, F. Liu, X. Wang, I. Datta, M. Lipson, A. Pan, X.-Y. Zhu, *Nat. Commun.* **2019**, *10*, 265.
[37] H. Haug, S. Schmitt-Rink, *Prog. Quantum. Electron.* **1984**, *9*, 3.
[38] K. Elkhouly, I. Goldberg, X. Zhang, N. Annavarapu, S. Hamdad, G. Croes, C. Rolin, J. Genoe, W. Qiu, R. Gehlhaar, P. Heremans, *Nat. Photonics* **2024**, 132.
[39] J. Butty, G. Bongiovanni, J. L. Staehli, *Phys. Status Solidi* **1995**, *188*, 199.
[40] F. Quochi, F. Cordella, A. Mura, G. Bongiovanni, F. Balzer, H.-G. Rubahn, *Appl. Phys. Lett.* **2006**, *88*.
[41] A. Simbula, R. Pau, F. Liu, L. Wu, S. Lai, A. Geddo-Lehmann, A. Filippetti, M. A. Loi, D. Marongiu, F. Quochi, M. Saba, A. Mura, G. Bongiovanni, *Energy Environ. Sci.* **2022**, *15*, 1211.
[42] K. Miyata, D. Meggiolaro, M. T. Trinh, P. P. Joshi, E. Mosconi, S. C. Jones, F. De Angelis, X.-Y. Zhu, *Sci. Adv.* **2017**, *3*, e1701217.
[43] G. D. Mahan, *Phys. Rev.* **1967**, *153*, 882.
[44] F. Sekiguchi, R. Shimano, *Phys. Rev. B* **2015**, *91*, 155202.
[45] P. Grivickas, V. Grivickas, J. Linnros, *Phys. Rev. Lett.* **2003**, *91*, 246401.
[46] T. Suzuki, R. Shimano, *Phys. Rev. Lett.* **2012**, *109*, 046402.
[47] C. Cho, A. Palatnik, M. Sudzius, R. Grodofzig, F. Nehm, K. Leo, *ACS Appl. Mater. Interfaces* **2020**, *12*, 35242.
[48] C. Klingshirn, *Semicond. Opt.* **2007**.
[49] A. Simbula, R. Pau, Q. Wang, F. Liu, V. Sarritzu, S. Lai, M. Lodde, F. Mattana, G. Mula, A. G. Lehmann, J. D. Spanopoulos, M. G. Kanatzidis, D. Marongiu, F. Quochi, M. Saba, A. Mura, G. Bongiovanni, *Adv. Opt. Mater.* **2021**, *9*, 2100295.
[50] S. Schmitt-Rink, D. S. Chemla, D. A. B. Miller, *Phys. Rev. B* **1985**, *32*, 6601.
[51] G. Findik, M. Biliroglu, D. Seyitliyev, J. Mendes, A. Barrette, H. Ardekani, L. Lei, Q. Dong, F. So, K. Gundogdu, *Nat. Photonics* **2021**, *15*, 676.
[52] M. Biliroglu, G. Findik, J. Mendes, D. Seyitliyev, L. Lei, Q. Dong, Y. Mehta, V. V. Temnov, F. So, K. Gundogdu, *Nat. Photonics* **2022**, *16*, 324.
[53] V. Ardizzone, F. Riminucci, S. Zanotti, A. Gianfrate, M. Efthymiou-Tsironi, D. G. Suàrez-Forero, F. Todisco, M. De Giorgi, D. Trypogeorgos, G. Gigli, K. Baldwin, L. Pfeiffer, D. Ballarini, H. S. Nguyen, D. Gerace, D. Sanvitto, *Nature* **2022**, *605*, 447.
[54] G. Xing, N. Mathews, S. S. Lim, N. Yantara, X. Liu, D. Sabba, M. Grätzel, S. Mhaisalkar, T. C. Sum, *Nat. Mater.* **2014**, *13*, 476.
[55] R. Su, C. Diederichs, J. Wang, T. C. H. Liew, J. Zhao, S. Liu, W. Xu, Z. Chen, Q. Xiong, *Nano Lett.* **2017**, *17*, 3982.